





High cooperativity coupling to nuclear spins on a circuit quantum electrodynamics architecture

Victor Rollano ^{1,2}, Marina C. de Ory ³, Christian D. Buch ⁴, Marcos Rubín-Osanz ^{1,2}, David Zueco^{1,2}, Carlos Sánchez-Azqueta ⁵, Alessandro Chiesa ^{6,7,8}, Daniel Granados ⁹, Stefano Carretta ^{6,7,8}, Alicia Gomez ³, Stergios Piligkos ⁴ & Fernando Luis ^{1,2}✉

Nuclear spins are candidates to encode qubits or qudits due to their isolation from magnetic noise and potentially long coherence times. However, their weak coupling to external stimuli makes them hard to integrate into circuit quantum electrodynamics architectures, the leading technology for solid-state quantum processors. Here, we study the coupling of $^{173}\text{Yb(III)}$ nuclear spin states in an [Yb(trensal)] molecule to superconducting cavities. Experiments have been performed on magnetically dilute single crystals placed on the inductors of lumped-element LC superconducting resonators with characteristic frequencies spanning the range of nuclear and electronic spin transitions. We achieve a high cooperative coupling to all electronic and most nuclear [$^{173}\text{Yb(trensal)}$] spin transitions, a necessary ingredient for the implementation of qudit protocols with molecular spins using a hybrid architecture.

¹Instituto de Nanociencia y Materiales de Aragón (CSIC - UNIZAR), 50009 Zaragoza, Spain. ²Departamento de Física de la Materia Condensada, Universidad de Zaragoza, 50009 Zaragoza, Spain. ³Centro de Astrobiología (CSIC - INTA), Torrejón de Ardoz, 28850 Madrid, Spain. ⁴Department of Chemistry, University of Copenhagen, DK-2100 Copenhagen, Denmark. ⁵Departamento de Física Aplicada, Universidad de Zaragoza, 50009 Zaragoza, Spain. ⁶Università di Parma, Dipartimento di Scienze Matematiche, Fisiche e Informatiche, I-43124 Parma, Italy. ⁷UdR Parma, INSTM, I-43124 Parma, Italy. ⁸INFN-Sezione di Milano-Bicocca, gruppo collegato di Parma, 43124 Parma, Italy. ⁹IMDEA Nanociencia, Cantoblanco, 28049 Madrid, Spain. ✉email: fluis@unizar.es

Recent efforts to build quantum computer hardware have given rise to small-scale processors with more than 100 qubits and to a staggering improvement of their operation fidelities and computing capabilities^{1–8}. Yet, reaching the conditions needed to perform large-scale computations remains a challenge for most existing platforms. The main reason is that correcting errors^{9,10} demands introducing a highly redundant encoding, thus significantly increasing the number of qubits needed for any practical implementation¹¹. A promising alternative is to use d -dimensional qudits as the building blocks^{12–14}. The extra levels can help simplify some quantum algorithms^{15–17} or quantum simulations¹⁸, ease their physical implementation and even provide a basis for embedding error correction in each single unit^{13,19–22}, which fulfils both the purpose of encoding information and accounting for errors resulting from quantum fluctuations.

Qudits have been realized with several physical systems, including photons^{23,24}, trapped ions²⁵, superconducting circuits²⁶, and electronic and nuclear spins^{27–29}. The latter are especially appealing, on account of their high degree of isolation from decoherence and the ability to control their spin states by means of relatively standard nuclear magnetic resonance (NMR) techniques³⁰. Not surprisingly, NMR experiments performed on nuclear spins of organic compounds in the solution provided some of the earliest implementations of quantum protocols^{31,32}. Very recently, nuclear spin states have also gained interest as a suitable platform to encode robust qubits in cold atoms trapped by lasers^{33,34}.

Exploiting nuclear spins as qudits in the context of circuit quantum electrodynamics (c-QED) is appealing, as the latter forms one of the most reliable platforms for solid-state quantum technologies^{35,36}. High cooperativity and even coherent or strong magnetic coupling have been achieved for electronic spin ensembles^{37–40}, thanks to a collective enhancement of the spin–photon interaction. Although some results suggest that it is possible to reach also quite high couplings between nuclear spins and photons in three-dimensional cavities⁴¹, the implementation in superconducting circuits remains challenging, mainly on account of the much weaker interaction of nuclear magnetic moments with electromagnetic radiation fields. An interesting possibility to overcome these limitations would be to use nuclear spin states of magnetic ions. The hyperfine interaction with the electronic spin mediates the coupling of nuclear spins to electromagnetic radiation fields^{42–44}, thereby enhancing nuclear Rabi frequencies with respect to those of isolated nuclei.

Here, we apply this idea to explore the coupling of on-chip superconducting resonators to the nuclear spins of magnetic molecules^{45–47}. We focus on one of the simplest realizations of a molecular qudit, [Yb(trensals)]^{42,48,49}, which hosts an individual Yb(III) ion ligated by an organic molecule. The ¹⁷³Yb isotope exhibits an $I = 5/2$ nuclear spin coupled to an effective electronic spin $S = 1/2$. The strong hyperfine interaction and the presence of a sizeable quadrupolar splitting, typical of lanthanide ions⁵⁰, give rise to the level of anharmonicity necessary for addressing the $(2S + 1) \times (2I + 1) = 12$ spin states and, therefore, to properly encode a $d = 12$ electronuclear spin qudit. The molecules form high-quality and high-symmetry single crystals in which all of them share the same axial orientation and where they can be diluted in an isostructural diamagnetic host in order to suppress decoherence. This introduces a collective enhancement of the coupling between molecular spin excitations and microwave photons, while preserving the ability to address individual spin transitions. This class of molecules has been recently proposed as a suitable platform to encode error-protected qubits^{21,28,42,44,51,52}. The experiments described in what follows were performed using novel, specifically designed lumped-

element resonators, whose properties can be fine-tuned to match the diverse nuclear and electronic spin transitions in this molecular system^{53–56}. The high-cooperativity regime between a nuclear spin ensemble and a superconducting resonator is achieved, with coupling strengths reaching fractions of MHz. Such coupling can be further enhanced by lowering the resonator's inductance and by isotopic enrichment of the crystal. Hence, these results show that the strong coupling regime for nuclear spin excitations is within reach and therefore provides a step towards the implementation of qudit algorithms within a solid-state hybrid scheme⁵⁷.

Results

Device description. Single crystals of [Yb(trensals)] doped into the isostructural diamagnetic host [Lu(trensals)] were obtained as described previously^{48,58}. The crystals contain all stable Yb isotopes, all of them with effective electronic spin $S = 1/2$ but different nuclear spin states I , in their natural abundances. Figure 1a, b show, respectively, the spin levels and resonant transition frequencies for [¹⁷³Yb(trensals)], with $I = 5/2$, for [¹⁷¹Yb(trensals)], with $I = 1/2$, and for all remaining isotopic derivatives with $I = 0$. For not too weak magnetic fields, nuclear spin transitions (between states characterized by the same m_S and $\Delta m_I = \pm 1$) have resonance frequencies below 1 GHz (Fig. 1b), whereas electronic spin transitions (between states characterized by the same m_I and $\Delta m_S = \pm 1$) occur at higher frequencies. To simplify the notation of resonant transitions, spin levels are labeled by a single index n in order of increasing energy at a high magnetic field (see Fig. 1a).

The interaction of cavity photons with the molecular electronic and nuclear spins is realized through a platform designed in the context of hybrid c-QED systems^{59,60}. A sketch of the device is shown in Fig. 1c. It consists of eight superconducting lumped-element LC resonators (LERs) coupled to a common readout transmission line. These LERs are designed with different resonance frequencies f_r , targeting different electronic and nuclear spin transitions. Since the LERs are parallel coupled to the transmission line, parameters such as resonance frequency and impedance can be freely designed without affecting the transmission through the device. Thus, as it is described in Supplementary Note 1, it is possible to tailor the microwave field $\mathbf{b}(\mathbf{r})$ generated by the inductor line in order to optimize the coupling rate per spin within the crystal volume. A contour plot of the field created by one of these resonators is included in Fig. 1c, next to the crystal and LER located on the right-hand side (see also Supplementary Fig. 1).

Different [Yb:Lu(trensals)] crystals, with concentrations x ranging from 2 to 8 %, were placed on top of each of the resonators. Typical crystal sizes were of order $1 \times 0.5 \times 0.5 \text{ mm}^3$ to match the size of the resonator inductances. The magnetic anisotropy axes lie parallel to the transmission line and to the external dc magnetic field \mathbf{B} . In this geometry, $\mathbf{b}(\mathbf{r})$ gives rise to finite transition rates between multiple pairs of spin states linked by nonzero matrix elements, as far as the spin energy levels are brought to resonance with the LER by the action of \mathbf{B} . Experiments have been performed with an input driving power of -95 dBm . This corresponds (see Supplementary Note 2) to a microwave photon number $\sim 10^8$, much lower than the number of spins involved in the coupling ($\sim 10^{16}$), thus avoiding power saturation effects (experiments aiming at the optimization of the driving power are shown in Supplementary Fig. 2).

Broadband spectroscopy. In order to identify the origin of the different resonances and to guide the design of the resonators, it is important to characterize the energy spectrum of the different Yb isotopes under the same conditions. To this aim, we

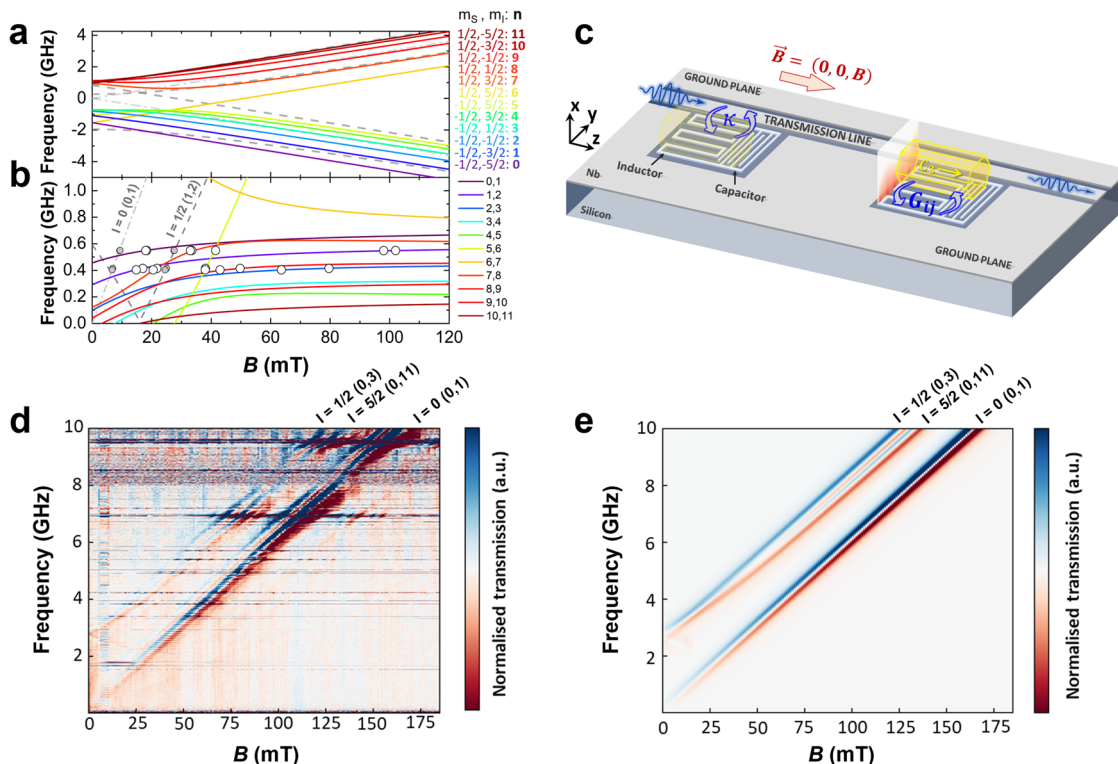


Fig. 1 Sample description and characterization. **a** Energy levels associated with the effective electronic S and nuclear I spin states of the different isotopical derivatives of [Yb(trensals)] molecules as a function of the magnetic field B . Solid colored lines correspond to [$^{173}\text{Yb}(\text{trensals})$] ($S=1/2$, $I=5/2$), dashed gray lines to [$^{171}\text{Yb}(\text{trensals})$] ($S=1/2$, $I=1/2$) and dashed-dotted gray lines to all remaining stable Yb isotopes having $S=1/2$ and $I=0$. The magnetic field is parallel to the C_3 crystal axis, which also defines a common magnetic anisotropy axis for all molecules. For sufficiently strong B , levels can be labeled by their electronic (m_S) and nuclear (m_I) spin projections, but at lower B both spins become entangled and this identification is no longer possible. In this work, we instead assign a single index n ($n=0, 1, \dots, (2S+1)(2I+1)$) to each level that follows the order of increasing energy at high B . **b** Frequency of resonant transitions between the different spin levels of all these derivatives as a function of a magnetic field. Only those lying below 1.1 GHz, which mainly correspond to nuclear spin transitions, are shown. Dots mark the frequencies and magnetic fields at which resonant transitions are observed in the experiments. **c** Scheme of an [Yb(trensals)] crystal (yellow) interacting with a superconducting circuit composed of several LC resonators with different characteristic frequencies, which are inductively coupled to a common readout superconducting transmission line. The latter line is parallel to the external dc magnetic field and to the crystal C_3 axis and can also be used to perform broadband magnetic spectroscopy on a single crystal located directly onto it. **d** Experimental results of on-chip broadband spectroscopy measurements for an [Yb:Lu(trensals)] crystal with a 7% Yb concentration. The normalized transmission derivative dS_{21}/dB , measured at 10 mK, provides a direct map of all spin excitations as a function of B and energy (or frequency). **e** Theoretical simulation of the normalized dS_{21}/dB . The conditions are the same as in **d**. Electronic spin transitions are clearly detected for the different isotopical derivatives. The labels in **d** and **e** mark transitions involving the ground spin state $n=0$ of [$^{171}\text{Yb}(\text{trensals})$] ($I=1/2$, 14% natural abundance), [$^{173}\text{Yb}(\text{trensals})$] ($I=5/2$, 14% natural abundance) and all remaining derivatives with $I=0$ (70% natural abundance).

performed experiments on an $x=7\%$ single crystal directly coupled to the superconducting readout transmission line (see Supplementary Fig. 3 for a sketch of this experimental configuration and additional results). These experiments allow us to address spin transitions at any possible driving frequency <14 GHz. The normalized transmission derivative $d|S_{21}(B, f)|/dB$ is shown in Fig. 1d as a function of magnetic field and driving frequency. Details on the normalization of the experimental data are described in Supplementary Note 3. The results provide a full picture of the Zeeman energy diagram. Resonances arising from the coupling to electronic spin transitions in [$^{173}\text{Yb}(\text{trensals})$] ($I=5/2$) and [$^{171}\text{Yb}(\text{trensals})$] ($I=1/2$), and to isotopes with zero nuclear spin are clearly visible. The comparison with theoretical simulations (see Fig. 1e and methods) reveals that the ratios between the intensities of these signals are 16, 14, and 70%, in good agreement with the natural abundances of the respective Yb isotopes. The half-width γ of the electronic transitions is ~ 23 MHz. This parameter characterizes the inhomogeneous broadening and it is the main limiting factor to reach a coherent coupling of the spins to the superconducting cavities^{37–40}.

Coupling cavity photons to multiple electronuclear spin transitions. The complex spin level spectrum of [$^{173}\text{Yb}(\text{trensals})$] and the presence of different Yb isotopes lead to multiple resonances of spin transitions n, n' with each of the resonators. Illustrative examples are shown in Fig. 2. The microwave transmission $|S_{21}|$ measured as a function of magnetic field and driving frequency at 10 mK shows clear signatures of the coupling to the spins, namely a shift of the cavity frequency and a drop in its visibility. The high-quality factor of these resonators leads to bare linewidths κ of the order of a few kHz, which contribute to very high sensitivity and allow resolving each of the individual transitions at their respective resonant fields. For frequencies above 1 GHz ($f_r = 2.93$ GHz in Fig. 2a), only electronic spin transitions contribute. Using the information about the field dependence of these spin levels obtained previously (Fig. 1), it is possible to assign all these features to specific electronic spin transitions of the different isotopes. As with the broadband spectroscopy results discussed above, the coupling to the more abundant $I=0$ isotopes shows the highest visibility. This agrees with the fact that the visibility of any spin resonance i, j increases with the collective

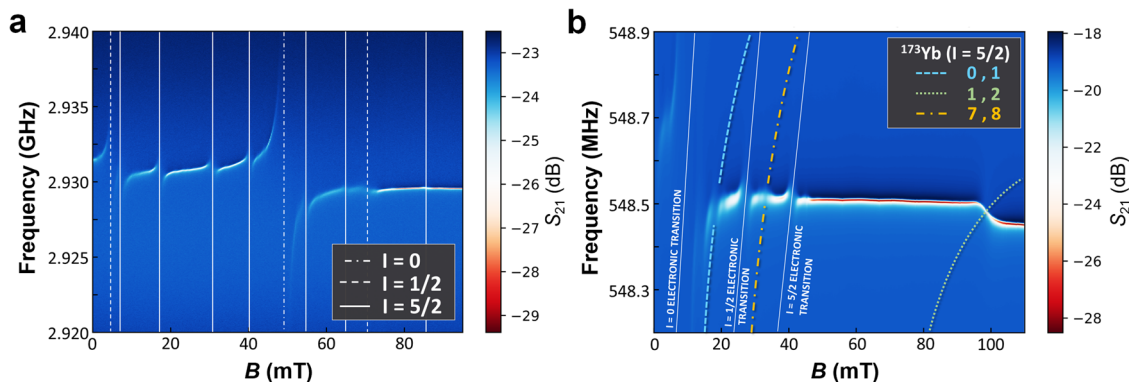


Fig. 2 Coupling cavity photons to multiple electronuclear spin transitions in [Yb(trensal)]. **a** Color plot of the microwave transmission measured at $T = 10$ mK near the bare resonance frequency $f_r = 2.93$ GHz of a LC superconducting resonator and as a function of the magnetic field. Changes in the resonator mark the coupling of cavity photons to different electronic spin transitions. The crystal had a $x = 5\%$ Yb nominal concentration. The lines assign each of the observed features to the different Yb isotopes naturally present in this crystal **b** Same as in **a** for a $f_r = 548.5$ MHz resonator and a crystal with $x = 8\%$. This LC cavity is specifically designed to optimally couple to nuclear spin transitions in [^{173}Yb (trensal)]. Some of them are identified in the caption. Color scale bars indicate the amplitude of the transmitted signal in relation to the input signal on a logarithmic scale.

spin-photon coupling $G_{i,j}$, which is proportional to $\sqrt{N_{i,j}}$, where $N_{i,j}$ is the number of spins involved in each particular transition.

For frequencies below 1 GHz, nuclear spin transitions from the isotopes having nonzero I are also observed. In particular, Fig. 2b shows the coupling of several nuclear spin transitions in [^{173}Yb (trensal)] to a $f_r = 548.5$ MHz superconducting cavity. These transitions are identified by their resonant magnetic fields and weaker visibility as compared to the electronic ones. Combining experiments performed on multiple resonators having different frequencies (in our case, $f_r = 403.6, 414.3, 548.5,$ and 549.5 MHz) allows tracking of how several of these transitions evolve with a magnetic field. These data were shown in Supplementary Fig. 4. Nuclear spin transitions are characterized by a much weaker magnetic field dependence, as expected (see Fig. 1b).

High cooperative coupling to electronic spins. Each of the observed transitions i, j can then be analyzed in detail, in order to determine the strength of the spin-photon coupling G_{ij} and the spin resonance linewidths $\gamma_{i,j}$. We first consider electronic spins. Figure 3a shows an illustrative example, taken from the low field region of Fig. 2a. This LER couples to the 0, 3 and 0, 11 electronic spin transitions of, respectively, [^{171}Yb (trensal)] ($I = 1/2$) and [^{173}Yb (trensal)] (our $I = 5/2$ qudit). A 2D least-squares fit of these experimental data, based on a generalized input-output model described in the methods section below, is shown in Fig. 3b. As can be seen in Fig. 3c and d, the fit reproduces very well the effect that the coupling to the spins has on the effective LER frequency \tilde{f}_r and resonance width $\tilde{\kappa}$, thus showing that this model provides a reliable description of the underlying physics.

The fit gives $G_{0,3} = 7.9$ MHz for [^{171}Yb (trensal)] and $G_{0,11} = 5$ MHz for [^{173}Yb (trensal)]. Values for other electronic transitions are shown in Supplementary Tables 1, 2. The linewidths are in good agreement with those derived from broadband spectroscopy experiments. They decrease with concentration, from about 22 MHz for $x = 8\%$ to 13 MHz for $x = 2\%$. The limit of strong coupling, defined by the condition $G_{i,j} > \kappa$ and $\gamma_{i,j}$ is only achieved for the $I = 0$ isotopes (see Fig. 2a, Supplementary Fig. 5, and Supplementary Table 1) for which $G_{0,1} = 22$ MHz, again as a consequence of their larger natural abundance. Still, all transitions measured reach the high cooperative coupling, characterized by a larger than unity cooperativity parameter $C_{i,j} \equiv (G_{i,j})^2 / (\gamma_{i,j} \cdot \kappa)$. For the transitions shown in Fig. 3, $C_{0,3} = 129$ and $C_{0,11} = 46$,

while for the $I = 0$ isotopes $C_{0,1}$ reaches 946. Reaching this limit implies that, at resonance, nearly every photon in the cavity is coherently transferred to the spin ensemble³⁷.

High cooperative coupling to nuclear spins. Reaching a similar condition with the nuclear spin states is, a priori, much more demanding on account of the very small nuclear magnetic moments. However, as we have mentioned above, the electronic spin introduces a quite efficient path to couple the nuclear spins to external magnetic fields. Therefore, it is to be expected that the same effect also enhances the coupling to cavity photons.

Figure 4a, b show experimental data for the 1, 2 and 2, 3 nuclear spin transitions in [^{173}Yb (trensal)], which are brought into resonance with a $f_r = 414.3$ MHz LER near 17 and 80 mT, respectively. The highest coupling rates for these transitions, $G_{1,2} = 0.24$ and $G_{2,3} = 0.11$ MHz, are achieved at 10 and 50 mK, respectively. Other nuclear spin transitions give comparable results (see Supplementary Table 3 and Supplementary Figs. 6, 7 for the complete set). For instance, the 0, 1 transition resonates with a 548.5 MHz LER at about 20 mT, as shown by Fig. 2b, with $G_{0,1} = 0.13$ MHz. The corresponding linewidths are $\gamma_{0,1} = 2.1$ MHz, $\gamma_{1,2} = 1.6$ MHz, and $\gamma_{2,3} = 0.6$ MHz, consistently with the effect of strain on quadrupole and hyperfine parameters. Indeed, the hierarchy between the $\gamma_{i,j}$ reflects the one between the derivatives of the corresponding gaps with respect to the Hamiltonian parameters $B, A_{x,z}$ and p (see Supplementary Figs. 8 and 9), pointing to inhomogeneous broadening as the origin of the observed linewidth. With a resonator half-width $\kappa \approx 3.78$ kHz, the high-cooperativity limit is achieved for all of them: $C_{0,1} = 2.0$, $C_{1,2} = 9.1$, and $C_{2,3} = 4.9$. The highest cooperativity has been achieved for the 1,2 resonance at $f_r = 403.3$ MHz and a relatively high Yb concentration $x = 8\%$, for which $G_{1,2} = 0.43$ MHz, $\gamma_{1,2} = 2.3$ MHz, and $C_{1,2} = 24.0$.

Although the couplings and cooperativities are about ten times smaller than what is achieved for the electronic transitions in the same molecular system, they are nevertheless remarkably high. If the nuclear and electronic spins were uncoupled, i.e., if the hyperfine interaction vanished, the nuclear spin-photon coupling would be mediated solely by the nuclear Zeeman interaction. As shown in Supplementary Fig. 10, this would lead to a ratio of about 10^{-4} between the coupling rates of nuclear and electronic transitions (say 1, 2 vs 0, 11). Therefore, the electronic spins help to mediate a much stronger interaction with the circuit photons.

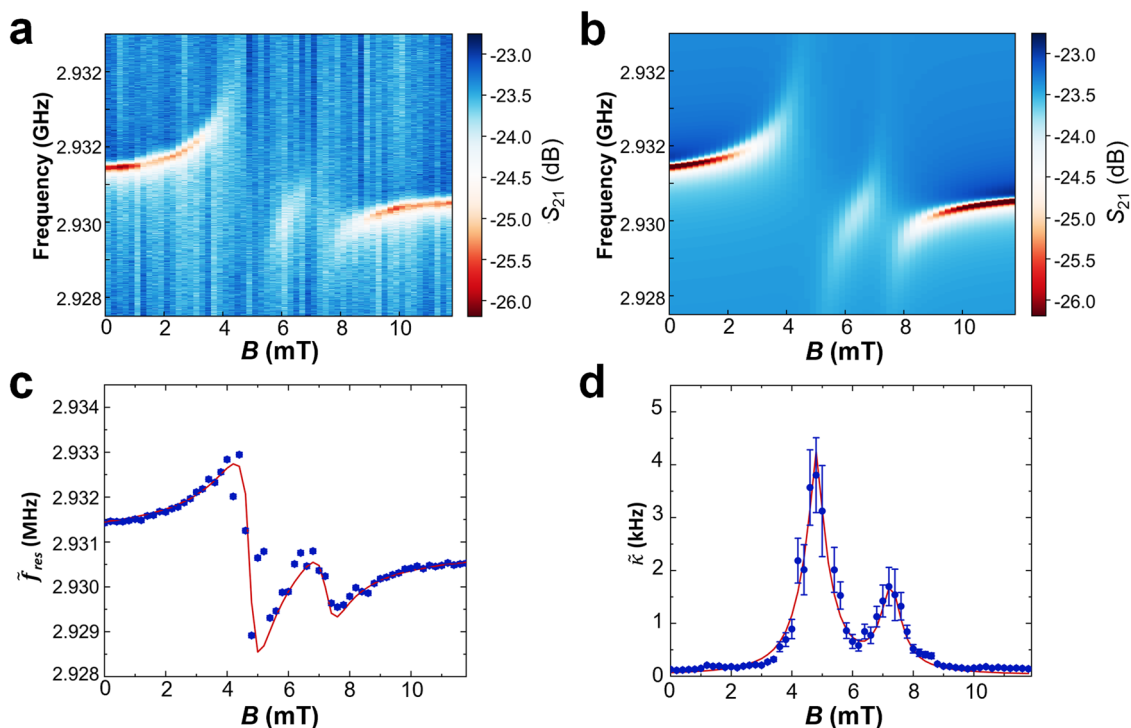


Fig. 3 Coupling cavity photons to the electronic spin. **a** Color plot of the microwave transmission measured at $T = 10$ mK near the bare resonance frequency $f_r = 2.93$ GHz of a superconducting lumped-element resonator (LER). The magnetic field brings the splittings between levels 0 and 3 of [$^{171}\text{Yb}(\text{trens})$] and 0 and 11 of [$^{173}\text{Yb}(\text{trens})$] into resonance with the cavity photons, leading to the observed crossings. **b** Optimized simulation of the experimental data shown in **a**, from which the collective spin–photon coupling and the spin line width are determined. Color scale bars indicate the amplitude of the transmitted signal in relation to the input signal on a logarithmic scale. **c** Resonance frequency (\tilde{f}_{res}) and **d** linewidth ($\tilde{\kappa}$) of the coupled spin–LER system as a function of the magnetic field, extracted from the experimental data (blue dots) and from the fit (solid red line). Errors have been determined from the Jacobian matrix obtained from the fits to Eq. (3).

Coupling rates of temperature dependence. Following the same procedure, we have determined the coupling constants of most detectable transitions as a function of temperature, which controls the relative populations of the electronuclear spin levels and, therefore, also the number of spins involved in the coupling to photons. Results obtained for electronic and nuclear spin transitions coupled to ~ 0.5 GHz LERs are shown in Fig. 5 (see also Supplementary Figs. 6 and 7). They are compared to numerical simulations based on the spin Hamiltonian of each species and on high-resolution 3D maps of the magnetic field generated by the LER (Fig. 1b and Supplementary Fig. 1). The only fitting parameter is an overall scaling factor that parameterizes the effective filling of the LER mode by the molecular crystal. The theory (see methods) reproduces fairly well the dependence of $G_{i,j}$ with T , although deviations are seen at the lowest temperatures. These mark the point where the relative spin level populations involved in each transition deviate from equilibrium. The fact that this happens at higher temperatures (of order 200 mK) for the nuclear spins than for the electronic spins (≤ 20 mK), suggests that the former have longer spin-lattice relaxation times T_1 . Together with the smaller linewidths observed for them (~ 1 – 2 MHz vs ~ 14 – 16 MHz for the electronic ones), this confirms that nuclear spins in [$^{173}\text{Yb}(\text{trens})$] remain less sensitive than the electronic ones to external perturbations and decoherence. In return, these results show that the initialization of the nuclear spin state needed for quantum implementations will probably require quite long thermalization times.

Time-resolved experiments. We have further investigated this point by means of time-resolved experiments, recording the charging and discharging of the resonator following the

application of square microwave pulses through the readout line. Results of transmission as a function of driving frequency and time are presented in Fig. 4c, d at two different magnetic fields corresponding to in and off-resonant conditions with the 1, 2 nuclear spin transition of [$^{173}\text{Yb}(\text{trens})$]. Additional data are shown in Supplementary Fig. 11. In the stationary state, attained near the end of the pulse duration, the response agrees perfectly well with the results measured with the continuous wave method. At shorter times, the response depends on the photon decay rate $\tilde{\kappa}$ and on how it is affected by the coupling to either electronic or nuclear spins. Figure 4d, e show that $\tilde{\kappa}$ becomes maximum whenever the photons become hybridized with the spins. Besides, the characteristic spin linewidth γ obtained near resonance is about ten times smaller for nuclear spin transitions than for electronic ones, at the same frequency, and agrees well with the value derived from continuous wave measurements.

Discussion

We have shown a high-cooperativity regime between nuclear spins and photons in an on-chip superconducting resonator setup. In particular, we have achieved this regime for both electronic and nuclear spin excitations in crystals of [$\text{Yb}(\text{trens})$] molecules. The hyperfine interaction with the electronic spin of the same ion plays here a key role as it enhances the interaction of nuclear spins to microwave magnetic fields, thus allowing them to reach the high-cooperativity regime without compromising their good isolation from noise^{42,44}. The balance between spin operation rates and coherence can furthermore be tuned by the magnetic field, which controls the degree of electronuclear spin entanglement⁴³. The results also exemplify the application of these devices to perform magnetic resonance at diverse

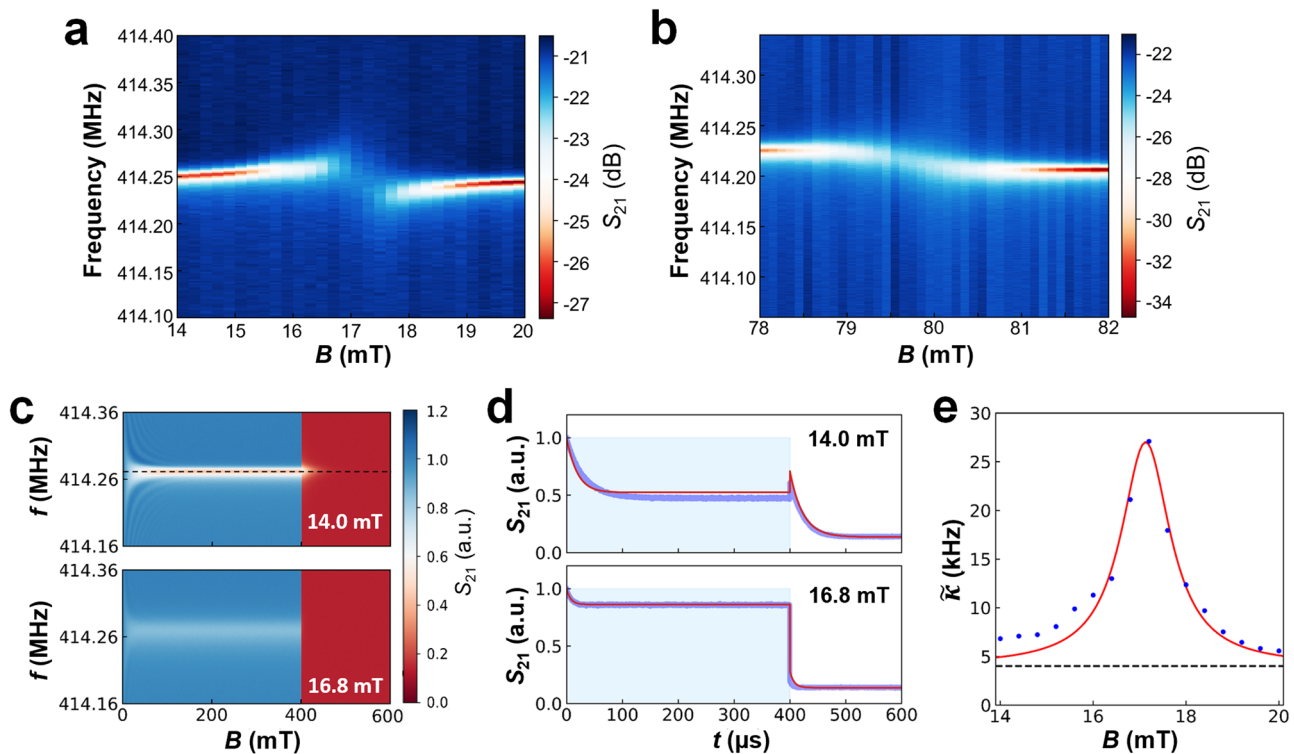


Fig. 4 Coupling cavity photons to nuclear spins. **a** Color plot of the microwave transmission showing the resonance of a $f_r = 414$ MHz superconducting lumped-element resonator (LER) to the 1, 2 nuclear spin transition in $[^{173}\text{Yb}(\text{trensal})]$. **b** Same as in **a** for the 2, 3 nuclear spin transition. Color scale bars indicate the amplitude of the transmitted signal in relation to the input signal on a logarithmic scale. **c** Time and frequency dependence of the transmission through the device normalized to the transmission of the bare readout line (see color scale bar on the right-hand side) and measured near the resonance of a $f_r = 414$ MHz LER following the application and removal of a $400 \mu\text{s}$ long pulse through the readout transmission line. The two plots show the behavior observed in and out of resonance with the 1, 2 nuclear spin transition in $[^{173}\text{Yb}(\text{trensal})]$. **d** Charging and discharging of the resonator were measured at constant driving frequencies near \tilde{f}_r and for the same magnetic fields. Dots are experimental results and lines are fits for a resonator with an effective photon decay rate $\tilde{\kappa}$ (see Supplementary Note 4, in particular, Supplementary Eqs. (5–7)). **e** Magnetic field dependence of $\tilde{\kappa}$ across the resonance with the 1, 2 nuclear spin transition. The solid line is a fit based on the input-output theory described in Supplementary Note 4, which allows deriving the nuclear spin linewidth $\gamma_{1,2} \approx 2.9$ MHz. Error bars in **e** are smaller than the data point size. They have been determined from the Jacobian matrix obtained from the fits based on Supplementary Eqs. (5–7).

frequencies and in a single experimental run, from which a complete characterization of multiple spin levels of different species (in our case, isotopical analogs of the same molecule) can be obtained.

Attaining a sufficiently high coupling of cavity photons to spin qubits and qudits is also crucial in order to exploit the latter either as quantum memories^{61,62} or as operational units of a hybrid processor^{57,63}. Even without reaching strong coupling, the circuit used in this work can serve as a basis for proof-of-concept realizations (on ensembles) of algorithms based on a qudit encoding. As proposed in refs. 21,22,42, a nuclear spin $I > 1$ coupled to an effective electronic spin 1/2 (of which $[\text{Yb}(\text{trensal})]$ is a prototypical realization) can be exploited to embed an error-protected logical unit within a single molecule. In the proposed setup, the control of nuclear spins, which encode the error-protected unit, can be done by introducing an extra excitation line and using conventional NMR techniques³⁰. Then, sufficiently high cooperativity would provide a way to dispersively read out the results⁶⁴.

Our results show that we are not far from reaching the strong coupling limit. Besides, they provide ample room for improving the spin–photon couplings. First, one can work with isotopically pure crystals containing only the most interesting $[^{173}\text{Yb}(\text{trensal})]$ molecules. For any concentration x , this introduces a collective enhancement of the coupling by a factor $\sqrt{1/0.16} \approx 2.5$ with respect to samples with natural isotopical abundances. Next, the

interface between the sample and the crystal also plays a very important role⁶⁵. The comparison of the measured coupling rates to theoretical simulations suggests that the filling factor of the cavity modes is as low as 4%, which is compatible with the existence of a gap of about $50 \mu\text{m}$ between the chip surface and the crystal (Supplementary Fig. 12). This leaves margin for a further factor 5 enhancement in $G_{i,j}$, perhaps even more, by exploiting the possibilities to design LERs adapted to the crystal sizes and geometries. For instance, one could work with smaller crystals coupled to resonators having correspondingly smaller inductor lines or, the opposite, use resonator designs leading to larger cavity volumes. Then, achieving a strong coupling regime seems feasible. In this regime, we expect γ to be further reduced, thanks to the cavity-protection mechanism^{66–68}. The strong coupling of an inhomogeneously broadened spin ensemble with the resonator introduces a gap between the bright and dark (subradiant) states, which protects the former from decay. This condition is met if the distribution of the spin ensemble frequencies decays faster than a Lorentzian, as typically found in NV center ensembles⁶⁷ and expected also here. An even more powerful alternative is that of engineering the lineshape of the spin ensemble by spectral hole burning techniques, see e.g., refs. 69–71.

Combined with suitable circuit designs^{72,73} and including nanometer-wide inductor lines in order to confine and locally enhance the microwave magnetic field⁷⁴, these ideas might even allow reaching sizeable couplings to individual nuclear spins, thus

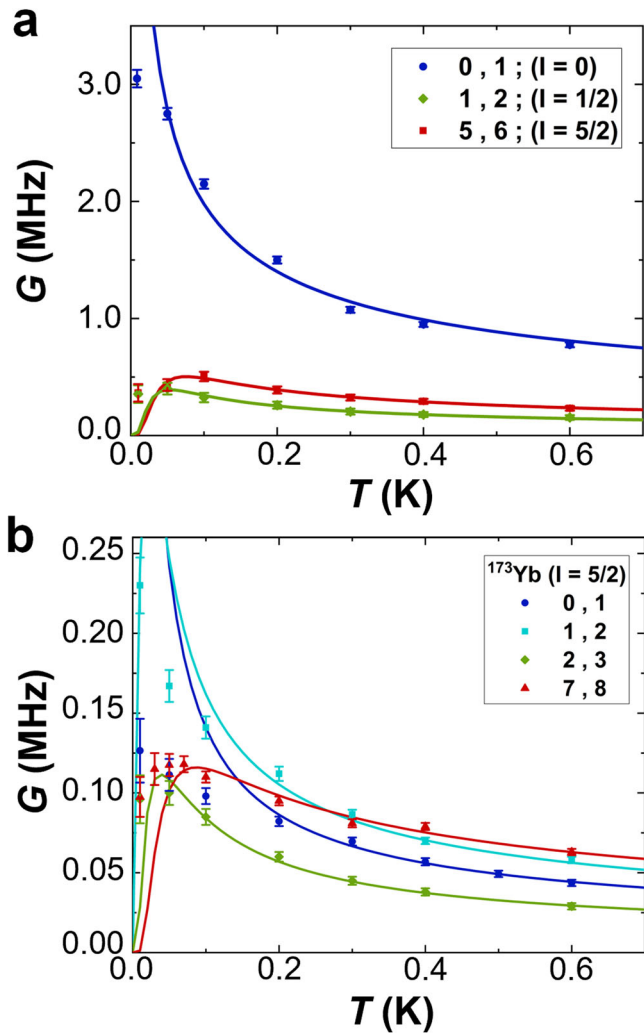


Fig. 5 Evolution of the spin-photon rates with temperature.

a Experimental (dots) and theoretical (lines) coupling rates as a function of temperature for the three electronic spin transitions coupled to a $f_r = 414.3$ MHz cavity. **b** Experimental (dots) and theoretical (lines) coupling rates as a function of temperature for different nuclear spin transitions in $[^{173}\text{Yb}(\text{trensals})]$. Here, the 0, 1 transition resonates at $f_r = 548.5$ MHz, while the others are measured with the same 414.3 MHz cavity as the electronic spin transitions shown in **a**. Errors have been determined from the Jacobian matrix obtained from the fits to Eq. (4).

opening the perspective of wiring up different nuclear spin qubits into a scalable architecture⁴⁷. In summary, the results offer many promising prospects for the integration and exploitation of nuclear spins in c-QED quantum architectures.

Methods

Experimental details. The superconducting cavities are based on a lumped-element resonators (LERs) design⁵⁶. They are fabricated by maskless lithography and reactive ion etching techniques on a 100-nm-thick Nb film deposited by means of DC magnetron sputtering on a 350 μm thick silicon substrate. The base pressure prior to the Nb deposition is better than 2.0×10^{-8} Torr. The cavities were designed using the commercial software Sonnet for the RF simulations and our CUDA code to calculate $b(\mathbf{r})$ (see Supplementary Note 1 and Supplementary Fig. 1).

Single crystals of $[\text{Lu}:\text{Yb}(\text{trensals})]$ (where $\text{H}_3\text{trensals} = 2,2,2$ -tris(salicylideneimino)-triethylamin) employed in these experiments consist of $[\text{Yb}(\text{trensals})]$ doped into the isostructural $[\text{Lu}(\text{trensals})]$ at different concentrations x . They were synthesized and grown over several weeks following a method described previously for $\text{Er}(\text{trensals})$ ⁵⁸, which employed a mixture of $\text{Yb}(\text{CF}_3\text{SO}_3)_3 \cdot 9\text{H}_2\text{O}$ and $\text{Lu}(\text{CF}_3\text{SO}_3)_3 \cdot 9\text{H}_2\text{O}$. The crystal and molecular structures were

characterized by X-ray diffraction of single crystals and powder samples (crashed single crystals), verifying their nature and purity. The complexes crystallize in the trigonal $\text{P}\bar{3}\text{C}1$ space group. The actual Yb concentration was determined by Inductively Coupled Plasma Mass Spectrometry (ICP-MS, Bruker Aurora Elite). The instrument was tuned prior to measurement and external calibration was performed using calibration points spanning the range of concentrations encountered in the samples. The nitric acid used was TraceSelect grade, and the reference material was provided by Inorganic Ventures. The sample was prepared by dissolving a single crystal from the same crystallization batch as the one providing the crystal for the experiments presented in 2% nitric acid (dissolved in 50 mL from which 0.125 mL was diluted to 50 mL). The sample preparation for ICP-MS and its analysis were performed at the Department of Chemistry, University of Copenhagen. Finally, the crystals were located on top of their respective superconducting LER. To improve the crystal-chip interface, we covered and gently pressed them with Teflon tape, fixed to the ground planes with low-temperature grease (Apiezon N). The chip was mounted in a BlueFors LD450 dilution refrigerator equipped with a 1 T superconducting magnet. A cold finger is used to place the chip in the center of the magnet. As shown in Supplementary Fig. 1, the microwave magnetic field created by the cavities is mostly perpendicular to the crystal anisotropy axis. The geometry of the setup is shown in Fig. 1c and Supplementary Fig. 3. The chip is connected through coaxial lines to a Vector Network Analyzer (VNA) with a measurement frequency bandwidth ranging from 10 MHz to 14 GHz. The device is then characterized by measuring the transmitted signal S_{21} .

Spin Hamiltonian. In our calculations, $[\text{Yb}(\text{trensals})]$ is described by the effective spin Hamiltonian:

$$\mathcal{H} = \mu_B \mathbf{S} \cdot g_S \cdot \mathbf{B} - \mu_N g_I \mathbf{I} \cdot \mathbf{B} + A_{\parallel} S_z I_z + A_{\perp} (S_x I_x + S_y I_y) + p I_z^2 \quad (1)$$

The first two terms correspond to the Zeeman coupling of electronic and nuclear spins, respectively, to the magnetic field. The A_{\parallel} and A_{\perp} terms describe the hyperfine coupling while the last term accounts for the quadrupolar interaction of the nuclear spin. Parameters for the three different Yb isotopes are summarized in Table 1.

Coupling of spins to a transmission line. The broadband spectroscopy experiments were analysed using an input-output theory for a 1D coplanar transmission line adapted to the conditions of our experiments. In this model, the coupling Γ_{ij} of a particular spin transition with resonance frequency (Ω_{ij}) to the photons with frequency f traveling through the transmission line is given by:

$$\Gamma_{ij} = 2\pi G \cdot \left| \langle \psi_j | \hat{V} | \psi_i \rangle \right|^2 \cdot \Delta P_{ij} \cdot \Omega_{ij} \cdot (n_{ij} + 1) \quad (2)$$

Where $G(f)$ is a spin-photon coupling density, which depends on the mode density in the transmission line and on a geometrical factor. The operator $\hat{V}(\mathbf{r}) = g_S \mu_B \mathbf{b}(\mathbf{r}) \cdot \mathbf{S} - g_I \mu_N \mathbf{b}(\mathbf{r}) \cdot \mathbf{I}$ mediates the interaction with the photons in the line at the position \mathbf{r} , ΔP_{ij} is the population difference between spin states i, j involved in the transition, and n_{ij} is the bosonic occupation number. Therefore, the transmission through the superconducting line is modeled as:

$$S_{21} = \frac{\alpha}{1 + \sum_{ij} \frac{\Gamma_{ij}}{y_{ij} + i(\Omega_{ij} - f)}} \quad (3)$$

Where α is a complex attenuation factor accounting for the dependence of the transmission line losses as a function of the driving frequency.

Spin-resonator coupling. For the resonator-spin case, the transmission probes the coupled system via the LC-resonator. The simplest model considers the two resonance frequencies, one for the spins Ω_{ij} and another one for the LC-resonator, f_r . The coupling between them is G_{ij} . In this case, S_{21} is computed by solving the set

Table 1 Parameters of the effective spin Hamiltonian for different $[\text{Yb}(\text{trensals})]$ isotopical derivatives.

	$g_{S\perp}$	$g_{S\parallel}$	g_I	A_{\perp} (GHz)	A_{\parallel} (GHz)	p (GHz)
^{171}Yb	2.935	4.225	-0.02592	3.3729	2.2221	0
$l=0\text{Yb}$	2.935	4.225	0	0	0	0
^{173}Yb	2.935	4.225	-0.02592	-0.615	-0.897	-0.066

The table shows the principal values (perpendicular, $g_{S\perp}$, and parallel, $g_{S\parallel}$, to the magnetic anisotropy axis) of the electronic spin g -tensor, the nuclear spin g_I factor, the principal values (perpendicular, A_{\perp} , and parallel, A_{\parallel} , to the magnetic anisotropy axis) of the hyperfine coupling tensor and the nuclear quadrupolar moment p .

of coupled equations

$$\begin{pmatrix} i(f_r - f) + \kappa & iG_{ij} \\ iG_{ij} & i(\Omega_{ij} - f) + \gamma_{ij} \end{pmatrix} \cdot \begin{pmatrix} b_1 \\ b_2 \end{pmatrix} = -i\sqrt{\kappa_e e^{i\varphi}} \begin{pmatrix} a_1 \\ a_2 \end{pmatrix} \quad (4)$$

and making $S_{21} = \alpha \cdot |1 - i\sqrt{\kappa_e e^{i\varphi}} \cdot b_1|$. Notice that since the system is driven through the superconducting cavity, $a_1 = 1$ and $a_2 = 0$. Actually, it is possible to obtain Eq. (3) from Eq. (4) with $G_{ij} = 0$ making $\kappa_e = \Gamma_{ij}$ and $\kappa - \kappa_e e^{i\varphi} = \gamma_{ij}$ (thus replacing the resonator with the spin ensemble).

The diagonal elements of the interaction matrix include the properties (resonance frequency and losses) of two oscillators: the superconducting LER (f_r, κ) and the i, j spin transition (Ω_{ij}, γ_{ij}). The off-diagonal elements depend on the coupling G_{ij} between these two oscillators. In our case, this parameter corresponds to the coupling rate of the spin ensemble to the microwave magnetic field generated by the LER. It is related to the coupling per spin \bar{G}_{ij} as follows: $G_{ij} = \sqrt{\int_V \bar{G}_{ij}^2}$,

where $\bar{G}_{ij} = |\langle \psi_j | \hat{V} | \psi_i \rangle| \cdot \Delta P_{ij}$. Finally, the resonator losses due to its coupling to the experimental setup (including the transmission line), are parameterized with a complex external loss rate ($\kappa_e e^{i\varphi}$) that multiplies both the driving and the transmission, and that also accounts for the asymmetries in the transmission signal⁵⁴. Using this model, the experimental data are then fitted for the whole frequency and dc magnetic field measurement ranges at once. The fit gives optimal values for κ, f_r, γ_{ij} , the field-dependent spin transition frequency $\Omega_{ij}(B) \equiv g_{\text{eff}} \mu_B B + \Omega_{ij}(0)$, and G_{ij} . The model can be expanded to several spin transitions coupled to the same LER by simply increasing the dimension of the interaction matrix accordingly. This allows characterizing each coupling individually even if the transitions are close to each other in a magnetic field (see Fig. 3a).

The coupling rate G_{ij} derived from the fits can be compared to the theoretical values in order to estimate the filling factor of the crystal-LER interaction. The theoretical coupling rate is calculated using the spatial distribution of the microwave magnetic field $b(r)$ obtained from the LER design. In the simulation, each cell with volume ΔV contributes with a coupling $\bar{G}_{ij}(r) = A\rho\Delta V|\langle \psi_j | \hat{V}(r) | \psi_i \rangle| \cdot \Delta P_{ij}$, where A is the isotopic abundance and ρ is the density of spins in the crystal. The theoretical coupling rate is then obtained by simply adding the contribution of every cell in the rf magnetic field simulation: $G_{ij} = \sqrt{\sum_k (\bar{G}_{ij}^k)^2}$.

Data availability

All data were available at the FATMOLS Zenodo repository <https://zenodo.org/communities/fatmols-fet-open-862893/about/>. <https://doi.org/10.5281/zenodo.6769030>.

Received: 30 March 2022; Accepted: 15 September 2022;

Published online: 06 October 2022

References

- Monz, T. et al. Realization of a scalable Shor algorithm. *Science* **351**, 1068–1070 (2016).
- Tacchino, F., Chiesa, A., Carretta, S. & Gerace, D. Quantum computers as universal quantum simulators: state-of-art and perspectives. *Adv. Quantum Technol.* <https://doi.org/10.1002/qute.201900052> (2019).
- Arute, F. et al. Quantum supremacy using a programmable superconducting processor. *Nature* **574**, 505 (2019).
- Arute, F. et al. Hartree-Fock on a superconducting qubit quantum computer. *Science* **369**, 1084–1089 (2020).
- Zhong, H.-S. et al. Quantum computational advantage using photons. *Science* **370**, 1460–1463 (2020).
- Wu, Y. et al. Strong quantum computational advantage using a superconducting quantum processor. *Phys. Rev. Lett.* **127**, 180501 (2021).
- Jurcevic, P. et al. Demonstration of quantum volume 64 on a superconducting quantum computing system. *Quantum Sci. Technol.* **6**, 025020 (2021).
- Pogorelov, I. et al. Compact ion-trap quantum computing demonstrator. *PRX Quantum* **2**, 020343 (2021).
- Devitt, S. J., Munro, W. J. & Nemoto, K. Quantum error correction for beginners. *Rep. Progr. Phys.* **76**, 076001 (2013).
- Terhal, B. M. Quantum error correction for quantum memories. *Rev. Mod. Phys.* **87**, 307–346 (2015).
- Fowler, A. G., Mariantoni, M., Martinis, J. M. & Cleland, A. N. Surface codes: towards practical large-scale quantum computation. *Phys. Rev. A* **86**, 032324 (2012).
- Gottesman, D., Kitaev, A. & Preskill, J. Encoding a qubit in an oscillator. *Phys. Rev. A* **64**, 012310 (2001).
- Pirandola, S., Mancini, S., Braunstein, S. L. & Vitali, D. Minimal qudit code for a qubit in the phase-damping channel. *Phys. Rev. A* **77**, 032309 (2008).
- Wang, Y., Hu, Z., Sanders, B. C. & Kais, S. Qudits and high-dimensional quantum computing. *Front. Phys.* **8**, 479 (2020).
- Lanyon, B. P. et al. Simplifying quantum logic using higher-dimensional Hilbert spaces. *Nature Phys.* **5**, 134–140 (2009).
- Kiktenko, E., Fedorov, A., Strakhov, A. & Man'ko, V. Single qudit realization of the Deutsch algorithm using superconducting many-level quantum circuits. *Phys. Lett. A* **379**, 1409–1413 (2015).
- Kiktenko, E. O., Fedorov, A. K., Man'ko, O. V. & Man'ko, V. I. Multilevel superconducting circuits as two-qubit systems: operations, state preparation, and entropic inequalities. *Phys. Rev. A* **91**, 042312 (2015).
- Tacchino, F., Chiesa, A., Sessoli, R., Tavernelli, I. & Carretta, S. A proposal for using molecular spin qudits as quantum simulators of light-matter interactions. *J. Mater. Chem. C* **9**, 10266–10275 (2021).
- Cafaro, C., Maiolini, F. & Mancini, S. Quantum stabilizer codes embedding qubits into qudits. *Phys. Rev. A* **86**, 022308 (2012).
- Michael, M. H. et al. New class of quantum error-correcting codes for a Bosonic mode. *Phys. Rev. X* **6**, 031006 (2016).
- Chiesa, A. et al. Molecular nanomagnets as qubits with embedded quantum-error correction. *J. Phys. Chem. Lett.* **11**, 8610–8615 (2020).
- Petiziol, F., Chiesa, A., Wimberger, S., Santini, P. & Carretta, S. Counteracting dephasing in molecular nanomagnets by optimized qudit encodings. *npj Quantum Inf.* **7**, 133 (2021).
- Lapkiewicz, R. et al. Experimental non-classicality of an indivisible quantum system. *Nature* **474**, 490–493 (2011).
- Chi, Y. et al. A programmable qudit-based quantum processor. *Nat. Commun.* **13**, 1166 (2022).
- Ringbauer, M. et al. A universal qudit quantum processor with trapped ions. *Nature Phys.* **18**, 1053–1057 (2022).
- Neeley, M. et al. Emulation of a quantum spin with a superconducting phase qudit. *Science* **325**, 722–725 (2009).
- Godfrin, C. et al. Operating quantum states in single magnetic molecules: implementation of Grover's quantum algorithm. *Phys. Rev. Lett.* **119**, 187702 (2017).
- Jenkins, M. D. et al. Coherent manipulation of three-qubit states in a molecular single-ion magnet. *Phys. Rev. B* **95**, 064423 (2017).
- Asaad, S. et al. Coherent electrical control of a single highspin nucleus in silicon. *Nature* **579**, 205–209 (2020).
- Vandersypen, L. M. K. & Chuang, I. L. NMR techniques for quantum control and computation. *Rev. Mod. Phys.* **76**, 1037–1069 (2005).
- Cory, D. G. et al. Experimental quantum error correction. *Phys. Rev. Lett.* **81**, 2152–2155 (1998).
- Vandersypen, L. et al. Experimental realization of Shor's quantum factoring algorithm using nuclear magnetic resonance. *Nature* **414**, 883–887 (2001).
- Jenkins, A., Lis, J. W., Senoo, A., McGrew, W. F. & Kaufman, A. M. Ytterbium nuclear-spin qubits in an optical tweezer array. *Phys. Rev. X* **12**, 021027 (2022).
- Ma, S. et al. Universal gate operations on nuclear spin qubits in an optical tweezer array of 171Yb atoms. *Phys. Rev. X* **12**, 021028 (2022).
- Blais, A., Huang, R.-S., Wallraff, A., Girvin, S. M. & Schoelkopf, R. J. Cavity quantum electrodynamics for superconducting electrical circuits: an architecture for quantum computation. *Phys. Rev. A* **69**, 062320 (2004).
- Blais, A., Grimsco, A. L., Girvin, S. M. & Wallraff, A. Circuit quantum electrodynamics. *Rev. Mod. Phys.* **93**, 025005 (2021).
- Schuster, D. I. et al. High-cooperativity coupling of electron-spin ensembles to superconducting cavities. *Phys. Rev. Lett.* **105**, 140501 (2010).
- Kubo, Y. et al. Strong coupling of a spin ensemble to a superconducting resonator. *Phys. Rev. Lett.* **105**, 140502 (2010).
- Kubo, Y. et al. Hybrid quantum circuit with a superconducting qubit coupled to a spin ensemble. *Phys. Rev. Lett.* **107**, 220501 (2011).
- Amsüss, R. et al. Cavity QED with magnetically coupled collective spin states. *Phys. Rev. Lett.* **107**, 060502 (2011).
- Abdurakhimov, L. V., Bunkov, Y. M. & Konstantinov, D. Normal-mode splitting in the coupled system of hybridized nuclear magnons and microwave photons. *Phys. Rev. Lett.* **114**, 226402 (2015).
- Hussain, R. et al. Coherent manipulation of a molecular Ln-based nuclear qudit coupled to an electron qubit. *J. Am. Chem. Soc.* **140**, 9814–9818 (2018).
- Gimeno, I. et al. Broad-band spectroscopy of a vanadyl porphyrin: a model electron nuclear spin qudit. *Chem. Sci.* **12**, 5621–5630 (2021).
- Chicco, S. et al. Controlled coherent dynamics of [VO(TPP)], a prototype molecular nuclear qudit with an electronic ancilla. *Chem. Sci.* **12**, 12046–12055 (2021).
- Atzori, M. & Sessoli, R. The second quantum revolution: role and challenges of molecular chemistry. *J. Am. Chem. Soc.* **141**, 11339–11352 (2019).
- Gaita-Ariño, A., Luis, F., Hill, S. & Coronado, E. Molecular spins for quantum computation. *Nature Chem.* **11**, 301–309 (2019).
- Carretta, S., Zueco, D., Chiesa, A., Gómez-León, A. & Luis, F. A perspective on scaling up quantum computation with molecular spins. *Appl. Phys. Lett.* **118**, 240501 (2021).

48. Pedersen, K. S. et al. Design of single-molecule magnets: insufficiency of the anisotropy barrier as the sole criterion. *Inorg. Chem.* **54**, 7600–7606 (2015).
49. Pedersen, K. S. et al. Toward molecular 4f single-ion magnet qubits. *J. Am. Chem. Soc.* **138**, 5801–5804 (2016).
50. Bertaina, S. et al. Rare-earth solid-state qubits. *Nature Nanotech.* **2**, 39–42 (2007).
51. Macaluso, E. et al. A heterometallic [LnLn'Ln] lanthanide complex as a qubit with embedded quantum error correction. *Chem. Sci.* **11**, 10337 (2020).
52. Lockyer, S. J. et al. Targeting molecular quantum memory with embedded error correction. *Chem. Sci.* **12**, 9104–9113 (2021).
53. Doyle, S., Mauskopf, P., Naylon, J., Porch, A. & Duncombe, C. Lumped element kinetic inductance detectors. *J. Low Temp. Phys.* **151**, 530–536 (2008).
54. Probst, S., Song, F. B., Bushev, P. A., Ustinov, A. V. & Weides, M. Efficient and robust analysis of complex scattering data under noise in microwave resonators. *Rev. Sci. Instrum.* **86**, 024706 (2015).
55. Weichselbaumer, S. et al. Quantitative modeling of superconducting planar resonators for electron spin resonance. *Phys. Rev. Appl.* **12**, 024021 (2019).
56. Aja, B. et al. Analysis and performance of lumped-element kinetic inductance detectors for W-band. *IEEE Trans. Microw. Theory Tech.* **69**, 578–589 (2021).
57. Jenkins, M. D. et al. A scalable architecture for quantum computation with molecular nanomagnets. *Dalton Trans.* **45**, 16682–16693 (2016).
58. Pedersen, K. S. et al. Modifying the properties of 4f single-ion magnets by peripheral ligand functionalisation. *Chem. Sci.* **5**, 1650–1660 (2014).
59. Xiang, Z.-L., Ashhab, S., You, J. Q. & Nori, F. Hybrid quantum circuits: superconducting circuits interacting with other quantum systems. *Rev. Mod. Phys.* **85**, 623–653 (2013).
60. Clerk, A. A., Lehnert, K. W., Bertet, P. & Nakamura, Y. Hybrid quantum systems with circuit quantum electrodynamics. *Nat. Phys.* **16**, 257–267 (2020).
61. Wesenberg, J. H. et al. Quantum computing with an electron spin ensemble. *Phys. Rev. Lett.* **103**, 070502 (2009).
62. Julsgaard, B., Grezes, C., Bertet, P. & Mølmer, K. Quantum memory for microwave photons in an inhomogeneously broadened spin ensemble. *Phys. Rev. Lett.* **110**, 250503 (2013).
63. Carretta, S. et al. Quantum information processing with hybrid spin-photon qubit encoding. *Phys. Rev. Lett.* **111**, 110501 (2013).
64. Gómez-León, Á., Luis, F. & Zueco, D. Dispersive readout of molecular spin qubits. *Phys. Rev. Appl.* **17**, 064030 (2022).
65. Urtizberea, A. et al. Vanadyl spin qubit 2D arrays and their integration on superconducting resonators. *Mater. Horiz.* **7**, 885–897 (2020).
66. Diniz, I. et al. Strongly coupling a cavity to inhomogeneous ensembles of emitters: potential for long-lived solid-state quantum memories. *Phys. Rev. A* **84**, 063810 (2011).
67. Putz, S. et al. Protecting a spin ensemble against decoherence in the strong-coupling regime of cavity QED. *Nat. Phys.* **10**, 720–724 (2014).
68. Chiesa, A., Santini, P., Gerace, D. & Carretta, S. Long-lasting hybrid quantum information processing in a cavity-protection regime. *Phys. Rev. B* **93**, 094432 (2016).
69. Krimer, D. O., Hartl, B. & Rotter, S. Hybrid quantum systems with collectively coupled spin states: suppression of decoherence through spectral hole burning. *Phys. Rev. Lett.* **115**, 033601 (2015).
70. Putz, S. et al. Spectral hole burning and its application in microwave photonics. *Nat. Photonics* **11**, 36 (2017).
71. Welinski, S. et al. Coherence time extension by large-scale optical spin polarization in a rare-earth doped crystal. *Phys. Rev. X* **10**, 031060 (2020).
72. Bienfait, A. et al. Reaching the quantum limit of sensitivity in electron spin resonance. *Nat. Nanotech.* **11**, 253–257 (2016).
73. Probst, S. et al. Inductive-detection electron-spin resonance spectroscopy with 65 spins/ Hz sensitivity. *Appl. Phys. Lett.* **111**, 202604 (2017).
74. Gimeno, I. et al. Enhanced molecular spin-photon coupling at superconducting nanoconstrictions. *ACS Nano* **14**, 8707–8715 (2020).

Acknowledgements

This work has been funded by the European Union Horizon 2020 research and innovation program through FET-OPEN grant FATMOLS-No 862893 and the QUANTERA project SUMO. It was also supported by the Spanish Ministry of Science and Innovation under grants RT2018-096075-B-C21, PCI2018-093116, PID2019-105552RB-C41 and C-44, PID2020-115221GB-C41/AEI/10.13039/501100011033, and Grant SEV-2016-0686 (MCIU/AEI/FEDER, UE) and by Novo Nordisk Foundation grant NNF20OC0065610. The SUMO project was also co-funded by the Italian Ministry of University and Research. We also acknowledge financial support from the Gobierno de Aragón grant E09-17R-Q-MAD, from CSIC Research Platform PTI-001, and from ONR-Global through Grant DEFROST N62909-19-1-2053.

Author contributions

C.D.B. and S.P. prepared and characterized the molecular crystals. M.C.d.O., D.G., and A.G. designed, modeled, and fabricated the chips. D.Z., M.R.-O., and V.R. developed the input-output theoretical model to analyze microwave transmission data. A.C. and S.C. developed the QEC protocol and characterized the spin states and levels of the molecular qubits. V.R., M.R.-O., and C.S.-A. performed and analyzed the microwave transmission experiments. F.L., S.P., D.Z., S.C., and A. G. conceived the idea. V.R. and F.L. wrote the manuscript with contributions from all co-authors.

Competing interests

The authors declare no competing interests.

Additional information

Supplementary information The online version contains supplementary material available at <https://doi.org/10.1038/s42005-022-01017-8>.

Correspondence and requests for materials should be addressed to Fernando Luis.

Peer review information *Communications Physics* thanks Shimon Kolkowitz and the other, anonymous, reviewer(s) for their contribution to the peer review of this work. Peer reviewer reports are available.

Reprints and permission information is available at <http://www.nature.com/reprints>

Publisher's note Springer Nature remains neutral with regard to jurisdictional claims in published maps and institutional affiliations.



Open Access This article is licensed under a Creative Commons Attribution 4.0 International License, which permits use, sharing, adaptation, distribution and reproduction in any medium or format, as long as you give appropriate credit to the original author(s) and the source, provide a link to the Creative Commons license, and indicate if changes were made. The images or other third party material in this article are included in the article's Creative Commons license, unless indicated otherwise in a credit line to the material. If material is not included in the article's Creative Commons license and your intended use is not permitted by statutory regulation or exceeds the permitted use, you will need to obtain permission directly from the copyright holder. To view a copy of this license, visit <http://creativecommons.org/licenses/by/4.0/>.

© The Author(s) 2022